ChemCatChem

The European Society Journal for Catalysis

Chemistry Europe

European Chemical Societies Publishing

Supported by

GECATS GERMAN CATALYSIS SOCIETY

Accepted Article

Title: Preparation of Alkali Metal Iridates as Oxygen Evolution Catalysts Via Thermal Transformation of Amorphous Iridium (oxy)hydroxides.

Authors: Mario Falsaperna, Rosa Arrigo, Frank Marken, and Simon Freakley

To be cited as: *ChemCatChem* **2024**, e202401326

Link to VoR: https://doi.org/10.1002/cctc.202401326

WILEY VCH

10.1002/cctc.202401326

Alkali Metal Iridates as Oxygen Evolution Catalysts *Via* Thermal Transformation of Amorphous Iridium (oxy)hydroxides.

Mario Falsaperna[1], Rosa Arrigo[2], Frank Marken[1], Simon J. Freakley[1*]

[1] *Department of Chemistry, University of Bath, Claverton Down, Bath, BA2 7AY, UK.*

[2] *School of Science, Engineering and Environment, University of Salford, M5 4WT Manchester, UK.*

Corresponding author s.freakley@bath.ac.uk

TOC

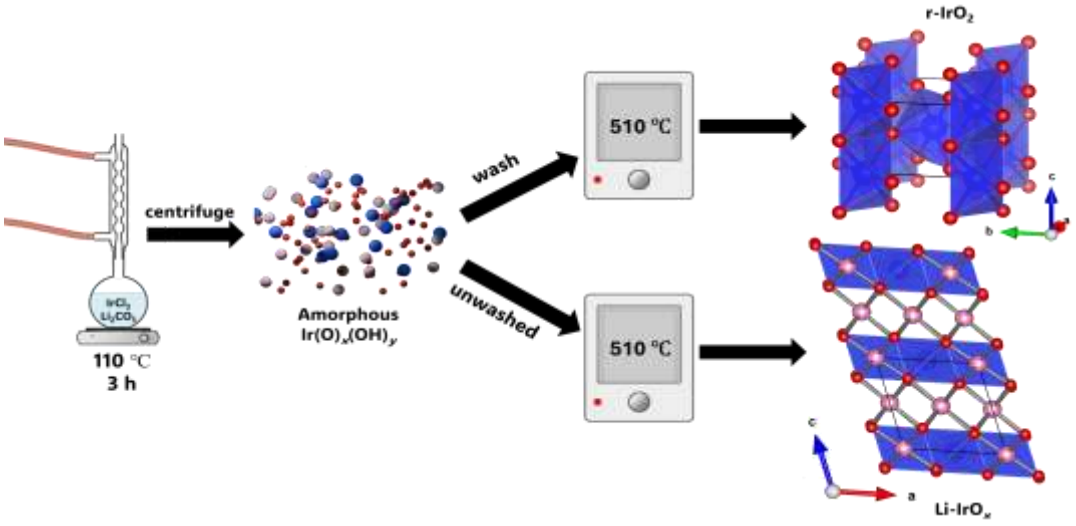

10.1002/cctc.202401326

Abstract

Efficient water-splitting is severely limited by the anodic oxygen evolution reaction (OER). Iridium oxides remain one of the only viable catalysts under acidic conditions due to their corrosion resistance. We have previously shown that heat-treating high-activity amorphous iridium oxyhydroxide in the presence of residual lithium carbonate leads to the formation of lithium-layered iridium oxide, suppressing the formation of low-activity crystalline rutile IrO_2. We now report the synthesis of Na-IrO_x and K-IrO_x featuring similarly layered crystalline structures. Electrocatalytic tests confirm Li-IrO_x reatins similar electrocatalytic activity as commercial amorphous $IrO_2{\cdot}2H_2O$ and with increasing size of the intercalated cation, the activity towards the OER decreases. However, the synthesised electrocatalysts that contain layers show greater stability than crystalline rutile IrO_2 and amorphous $IrO_2{\cdot}2H_2O$, suggesting these compounds could be viable alternatives for industrial PEM electrolysers where durability is a key performance criterion.

Introduction

To transition to a hydrogen economy, efficient water electrolysis is crucial to storing renewable energy.[1] The anodic oxygen evolution reaction (OER) under acidic conditions can often limit the overall performance of electrolyser devices due to high kinetic barriers requiring additional overpotential (η), leading to energy losses and inefficiency.[2] A second challenge is to find catalysts that can operate under the required anodic potentials in an acidic environment without rapid deactivation through passivation or corrosion.[3] To date, RuO_2 and IrO_2 are the most studied materials for OER under acidic conditions.[4–6] The former displays high activity but shows low stability due to fast corrosion in acidic media. The relationship between stability and activity of various IrO_2 morphologies has been extensively studied in recent years.[7] Colloidally prepared metallic Ir nanoparticles or deposited Ir metallic films have been shown to readily form amorphous iridium(oxy)hydroxide ($Ir(O)_x(OH)_y$) surfaces under OER conditions which is the active form of the catalyst.[8,9] $Ir(O)_x(OH)_y$ outperforms highly crystalline rutile IrO_2 (r-IrO_2) in terms of reduced overpotential (η) and amorphous $Ir(O)_x(OH)_y$ materials have been shown to convert to rutile IrO_2 under thermal treatments >350 °C during preparation. Geiger *et al.* reported that annealing amorphous $Ir(O)_x(OH)_y$ films results in rutile IrO_2 with reduced intrinsic activity, suggesting a fine balance between activity, stability, and structure of the catalyst.[10] Using atom probe tomography to study the structural evolution of Ir oxides gives evidence for oxygen mobility/exchange with the electrolyte during the OER using isotopically labelled $Ir^{18}O_2$.[11] These results suggest that structural flexibility plays a key role in the activity of iridium oxides but may also trigger deactivation through corrosion.[12] Crystalline IrO_2 has been generally shown to have lower activity but greater stability towards OER compared to the amorphous analogue.[13]

The development of both active and stable IrO_2 catalysts remains a significant challenge and has been studied *via* a wide array of synthetic methods to control the morphological features of the material. Recently the role of alkali metals in both the OER electrolyte and the catalyst material has gained increasing attention.[14] Koper *et al.* recently demonstrated that the addition of Li^+ to a NaOH electrolyte increases the rate of OER over NiFe(OOH) catalysts by enhancing the mass transport of water through the structure.[15] Furthermore, we recently demonstrated higher ECSA normalised OER activity of iridium(oxy)hydroxides synthesised in the presence of alkali metal salts, such as Li_2CO_3 compared to commercial materials which had comparable geometric surface areas, surface atomic and electronic composition, and bulk structures.[16] It was found that materials prepared with bases containing Li^+ cations led to amorphous $Ir(O)_x(OH)_y$ showing a significantly lower overpotential (η = 250 mV at 10 mA cm^{-2}) and increased stability compared to commercail rutile IrO_2 or amorphous $IrO_2 \cdot 2H_2O$. This higher activity, normalized to active electrochemical surface area (ECSA), suggested a possible promotional effect of residual alkali metal ions. Gao *et al.* synthesised a similar amorphous Li^+-doped IrO_x catalyst with high activity (η = 270 mV at 10 mA cm^{-2}) suggesting that the presence of Li^+ promotes flexible IrO_6 octahedra.[17] Alkali-doped crystalline hollandite IrO_2 structures have also been reported by

Sun *et al.* who synthesized $K_{0.25}IrO_2$ from $IrCl_3/K_2CO_3$ by annealing in air (600 °C, 6 h), and distorted IrO_6 octahedra were suggested to increase activity compared to rutile IrO_2.[18]

Recently our group have shown that when amorphous $Ir(O)_x(OH)_y$ contains residual Li^+ from the hydrothermal precipitation the thermal conversion to low-activity rutile IrO_2 at 300-400 °C can be suppressed. Instead, on heat treatment a nanocrystalline Li-intercalated iridium oxide (Li-IrO_x) forms at relatively mild conditions (500 °C, 3 h).[19] These Li-IrO_x electrocatalysts exhibit comparable activity and improved stability compared to the commercially available $IrO_2.2H_2O$, indicating this nanocrystalline iridate structure could be more practical for industrial applications where higher durability is necessary. In the present study, we show that starting from amorphous $Ir(O)_x(OH)_y$, it is possible to prepare alkali layered iridate materials containing Li^+, Na^+ and K^+ by adopting the same synthetic approach and retaining residual alkali metal salts, *i. e.* Li_2CO_3, Na_2CO_3, K_2CO_3. We find the activity of the electrocatalysts is not improved when adding heavier alkali metals. However, these materials show higher stability than amorphous alkali metal-free iridium oxide and could be viable alternatives for more durable catalysts in industrial applications.

Experimental

Synthesis of Iridium Materials - Amorphous iridium oxyhydroxide, $Ir(O)_x(OH)_y$, was prepared following the method reported previously.[16] 1 mmol $IrCl_3$ hydrate (Johnson Matthey) and 8 mmol of M_2CO_3 (M = Li^+, Na^+ and K^+, 99.0+% Sigma Aldrich, 99% Thermoscientific and 99.5% Thermoscientific, respectively) were dissolved in 10 mL of deionized water and stirred for 16 h at 25 °C. 10 mL of deionized water was added, followed by reflux for 3 h. The mixture was cooled to room temperature and the precipitate was recovered by centrifugation and dried at 60 °C for 16 h. Metal-doped iridium oxides, M-IrO_x (M = Li^+, Na^+ and K^+) were obtained by heat treating the precursor $Ir(O)_x(OH)_y$ containing the M_2CO_3 (M = Li^+, Na^+ and K^+) in static air at temperatures between 510 and 525 °C for 3 h. Residual M_2CO_3 and Cl contamination were removed by washing with 1 L of hot and 1 L of cold deionised water *via* centrifugation. Finally, the solid obtained was dried overnight at 60 °C.

Catalyst Charcteristion - Powder X-ray Diffraction (XRD) patterns were obtained on a Stoe Stadi P powder diffractometer in transmission mode fitted with a Multi-MYTHEN detector and using a Cu Kα radiation source (λ = 1.5046 Å, 40 keV, 40 mA). The Harwell JEOL-ARM2000 Aberration-Corrected Transmission Electron Microscope was used to analyse the M-IrO_x electrocatalysts at 200 kV electron beam, with samples ground and dusted onto carbon-coated Cu TEM grids in bright field and high angular annular dark field (HAADF) STEM modes, as well as in TEM mode. Scanning electron microscopy (SEM) measurements were performed using a Hitachi SU3900 microscope. Powder samples were deposited on carbon tabs placed on aluminium sample holders, followed by gold coating. Images were acquired using a 10 kV electron beam and employing both a backscattering electron (BSE) and a secondary electron (SE) detector. Ir 4f and O1s X-ray photoelectron spectra (XPS) were obtained

using a Thermo Fisher Scientific K-alpha+ spectrometer. Samples were analysed using a micro-focused monochromatic Al X-ray source (72 W) using an elliptical X-ray spot of ca. 400 x 600 microns. Data was recorded at pass energies of 150 eV for survey scans and 50 eV for high-resolution scans with 1 eV and 0.1 eV step sizes respectively. Charge neutralisation of the sample was achieved using low-energy electrons and argon ions. Fitting of the XPS data was carried out using the model summarised in Table S3, and following the Levenberg–Marquardt algorithm to minimize χ^2. Background correction was performed using a Shirley background. The O K-edge NEXAFS spectra were collected at the B07 beamline at the UK synchrotron facility Diamond Light Source (DLS) using a 400 l/mm Au grating of the monochromator.[20] The exit slit (ES) was set to 0.5 μm x 0.04 μm and the fix focus constant (cff) to 2.0. Spectra were collected in total electron yield mode by detecting the drain current generated by the photoemitted electrons from the samples at a distance of approximately 200 μm. In Auger yield mode data were collected using the electron analyser of the VERSOX end station at DLS, setting the kinetic energy to 395 eV and pass energy 100 eV. Spectra were normalized to the maximum intensity at approximately 546 eV, after linear background subtraction. The relative energy calibration of the spectra was checked using features in the drain current of the beamline nozzle, and fixing the μ_3-O resonance of r-IrO_2 to 530 eV.

XAS were recorded in transmission mode at the Ir L3 edge, at the B18 beamline of the Diamond Light Source. Pellets were prepared by grinding powders with cellulose as a matrix for *ex situ* analysis. Working electrodes for *in situ* XAS measurements were prepared *via* drop-casting 47 μL of catalyst ink (5 mg catalyst in 2 mL of water, 0.5 mL of methanol) on a 12 mm TorayTM carbon paper TGP-60 to obtain catalyst loading of ~100 μg_{cat} cm^{-2}. 1 μL Nafion 5 %wt was deposited on top of the catalyst ink once this was dry. Three scans per sample were recorded, and the averaged signal was used for data analysis. The measurements were performed using a QEXAFS setup with a fast-scanning Si (111) double crystal monochromator. For the *in situ* measurements, the time resolution of the data acquisition was ~200 s/spectrum. XANES and EXAFS data were interpreted using IFEFFIT with Demeter software package (Athena and Artemis),[21] using structural models available from ICDD as cited in the text. *In situ*, XAS measurements were carried out using a sealed cell filled with a 0.1 M $HClO_4$ and with catalyst inks deposited on carbon paper as working electrodes. A Pt wire and a Ag/AgCl electrode were used as counter and reference electrodes, respectively.

Catalyst Testing - Catalysts were tested on a three-electrode setup in a 0.1 M $HClO_4$ (Honeywell, 70%) electrolyte using a Biologic SP-300 potentiostat. A coiled Pt wire (127 μm diameter, 99.99%, Advent Research Materials) was used as the counter electrode, a rotating disk glassy carbon electrode (5.00 mm disk diameter, 0.196 cm^2 geometric surface area, model AFE5T050GC, Pine Research) was used as the working electrode, and a Ag/AgCl electrode (ALS Co. Ltd., model RE-1B, $E^0_{Ag|AgCl} = +0.195\ V_{RHE}$) was used as the reference electrode. To prepare the catalyst ink, 5 mg of catalyst, 2.0 mL of water, 0.5 mL of methanol was sonicated for 30 min. 20 μL of the catalyst ink was drop-cast onto the GC working

electrode and dried under an IR lamp. The catalyst activity toward OER was measured by linear sweep voltammetry (LSV, 0.2 to 1.8 V_{RHE} at 5 mV s^{-1}), at room temperature. The current densities in the LSV plots were obtained by normalising the measured currents by the electrode geometric surface area. Catalyst stability was assessed by chronopotentiometry (CP, 2 h and 25 h, at 10 mA cm^{-2}). The double-layer capacitance (C_{DL}) was obtained from CVs in the 0.4–0.5 V_{RHE} region at different scan rates (2, 5, 10, 40, 80, and 100 mV s^{-1}). The ECSA was obtained by dividing the C_{DL} by the specific capacitance in acid media ($C_{s,ac}$ = 0.035 mF cm^{-2}) and the roughness factor (Rf) was calculated by dividing this by the geometric surface area. Tafel slopes were derived from semi-steady-state conditions obtained from LSV measurements performed at low overpotential (1.43–1.56 V_{RHE}, 0.5 mV s^{-1})**.** Reported values are expressed against the reversible hydrogen electrode (RHE), with values obtained according to $E_{RHE} = E_{Ag/AgCl} + E^0_{Ag/AgCl} + (0.059V \times pH)$, and with the pH M $HClO_4$ measured as ~1.

Results and Discussion

The facile synthesis of amorphous $Ir(O)_x(OH)_y$ using Li_2CO_3 as a precipitating agent produced an active and relatively stable IrO_x material compared to commercial $IrO_2 \cdot 2H_2O$ when tested under our experimental conditions (see experimental section). We demonstrated that by retaining residual Li_2CO_3 in the parent material by omitting a washing step, the thermal transition to rutile IrO_2 (r-IrO_2) at ~ 400 °C under air is suppressed and instead, a nano-crystalline lithium iridate is formed (see **Scheme 1**).[19]

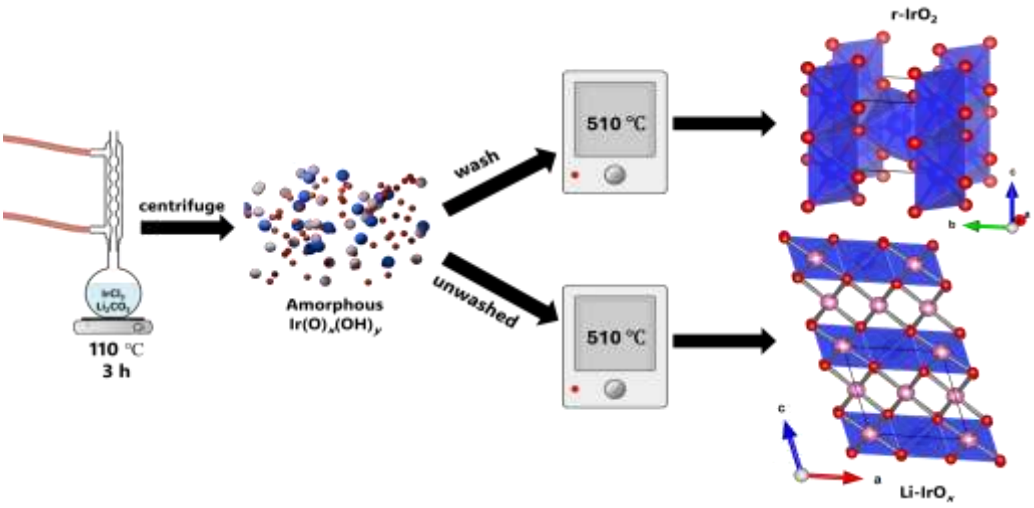

Scheme 1 - Synthesis of $Ir(O)_x(OH)_y$ with Li_2CO_3 as a precipitating salt, followed by the divergent routes for the synthesis of r-IrO_2 or Li-IrO_x. Blue, red and pink atoms represent iridium, oxygen and lithium, respectively.

Both β-Li_2IrO_3 and α-Li_2IrO_3 contain layered Ir-oxo sheets made predominantly from Ir-O_6 octahedra with both in-plane and interlayer Li^+ with characteristic interlayer spacings of ~0.48 nm consistent with x = 2.[22] Lithium iridate preparation methods typically involve the use of high-temperature solid-state or molten salt synthesis with prolonged reaction times, *e.g.* β-Li_2IrO_3 synthesis was reported previously

by treating Ir/IrO_2 and Li_2CO_3 at 1080 °C for 30 h or heating $IrCl_3$ in molten LiOH at 700-900 °C.[23–25] In this case, we propose starting from an amorphous $Ir(O)_x(OH)_y$, which has higher structural flexibility than crystalline Ir black or r-IrO_2, making this solid state reaction/transition more facile with the intimately mixed $Ir(O)_x(OH)_y/Li_2CO_3$ product of the precipitation.

Initially, we synthesised amorphous $Ir(O)_x(OH)_y$ using Li_2CO_3, Na_2CO_3 and K_2CO_3 as precipitating agents using identical procedures. X-ray diffraction (see **Figure 1a-c**) shows that the as-synthesised materials remain amorphous with only broad diffraction features at ~35° before any thermal treatment. Additional contaminant diffraction features were consistent with the respective residual metal carbonates. The three $Ir(O)_x(OH)_y$ samples containing residual Li^+, Na^+ and K^+ were subsequently calcined under static air at for 3 h 510, 500 and 525 °C for Li-IrO_x , Na-IrO_x and K-IrO_x respectively. The heat treatment in the presence of residual alkali metal carbonates suppressed the formation of rutile IrO_2 in each case and led to the formation of layered iridium oxide structures. In particular, low angle reflections develop at 2θ angles, ~19°, ~17° and ~13° for M = Li^+, Na^+ and K^+ respectively. The interlayer *d*-spacing values corresponding to those reflections are 4.7, 5.0 and 6.9 Å for M = Li^+, Na^+ and K^+ correlating with the increasing size of the incorporated alkali metal cation. The interlayer distance found for Li-IrO_x is consistent with previous results and the β-Li_2IrO_3 phase reported by O'Malley *et al.* who prepared samples by heating Li_2CO_3 and Ir metal at 750 °C 12 h before the increasing temperature to 1050 °C [ICSD-246025].[26] It should be noted that the synthesis of K-IrO_x was successful only when a large excess of K_2CO_3 (~10x) was ground with the synthesised $Ir(O)_x(OH)_y$ before annealing. By contrast, the synthesis of Li-IrO_x and Na-IrOx required no additional carbonates other than those use in the precipitation step before thermal treatment.

To confirm the presence of the layered phases, refinements of structural models were carried out using the Le Bail method.[27] Structural models for previously reported lithium iridate (Li_2IrO_3) and sodium iridate (Na_2IrO_3), both featuring a monoclinic *C*2/*m* structure,[26,28] as well as for potassium iridate ($K_{0.3}IrO_2{\cdot}0.6H_2O$), featuring a trigonal $R\bar{3}m$ structure,[29] show good agreement with the data (see **Figure 1d-f, Supplementary Table 1**). It should be noted that the diffraction patterns for Li-IrO_x and Na-IrO_x feature broad reflections, indicating these materials consist of nanocrystalline domains. In contrast, K-IrO_x features sharper reflections, indicating larger crystallites. Applying the Scherrer equation to the lowest angle reflections allows the determination of average crystallite dimensions, with their sizes having values of ~3, ~7 and ~36 nm for Li-IrO_x, Na-IrO_x and K-IrO_x, respectively.[30] Low magnification scanning electron microscopy (SEM) of *M*-IrO_x (*M* = Li^+, Na^+, K^+) (see **Figure 2 a-c**) shows that the Li- and Na-IrO_x have no distinct morphological features whereas the K-IrO_x shows needle-shaped particle morphology (see **Figure 2c**). High-resolution aberration-corrected transmission electron microscopy (HR-TEM) suggests that Li-IrO_x is polycrystalline with nanocrystalline domains, consistent with previous findings and similar to the Na-IrO_x sample. By contrast, TEM images of the K-IrO_x

suggest this material features significantly larger crystallite domains supporting our observations from the powder XRD patterns for each compound.

The bulk electronic structure of the series was studied by X-ray absorption spectroscopy at the Ir L_3-edge. The near edge region of the absorption spectrum is characterised by a resonance corresponding to a $2p_{3/2} \rightarrow 5d$ electronic transition, generally referred to as the white line (WL), which is sensitive to absorber symmetry, ligand environment, and oxidation state (d-state occupancy). **Figure 3a** shows that r-IrO_2, $IrO_2 \cdot 2H_2O$, and the synthesised metal iridates have similar white line positions (11,218.6–11,219.3 eV) defined by the minimum in the second derivative. Comparison of Ir^0 ($5d^7$), $IrCl_3$ ($5d^6$), and IrO_2 ($5d^5$) (see **Figure S1**) suggests a mixed valance Ir(IV)/Ir(III) species with average formal oxidation states of ~$Ir^{+3.7}$ for $IrO_2 \cdot 2H_2O$ and the synthesised metal iridates thought to be associated with some degree of hydration in the samples when considering commercial IrO_2 as a reference for $Ir^{+4.0}$. This higher bulk oxidation state of commercial rutile IrO_2 is supported by a shift to higher energy of the absorption edge compared to the other materials studied (inset **Figure 3a**). Fourier-transformed EXAFS (non-phase corrected) are shown in **Figure 3b**. All samples show 1st shell scattering intensity consistent with Ir-O_x coordination in the 1st shell, fitting a single Ir-O scattering path (see **Table 1**) suggests that all samples could be considered to have an Ir-O_6 coordination with CN ~6.[31] For the samples which show formal oxidation state <$Ir^{4.0}$ the Ir-O bond is ~2.01 Å compared to 1.98 Å for rutile IrO_2 consistent with a lower average oxidation state of the Ir centre. Considering the 2nd coordination shell which for rutile IrO_2 consists of two Ir-Ir and additional Ir-O scattering paths the synthesised iridates (which also include the possible effects of light scattering elements) show different long-range structures when considering the scattering intensity between 2.5 – 4 Å and the k-space phasing **(Figure S2)**.[32,33] This intensity suggests that rather than the regular edge and corner-sharing Ir-O_6 units in crystalline rutile materials, the layered iridates have shorter Ir-Ir_1 and Ir-Ir_2 coordination shells.

The OER activity of the commercial standards, r-IrO_2 and amorphous $IrO_2 \cdot 2H_2O$, and the synthesised *M*-IrO_x samples (*M* = Li^+, Na^+ and K^+) in 0.1 M $HClO_4$ was assessed by LSV (0.2 – 1.8 V_{RHE}, 5 mV s^{-1}) (see **Figure 4a-d**). Amorphous $IrO_2 \cdot 2H_2O$ exhibits the greatest activity towards OER, reaching a current density of ~67 mA cm^{-2} at 1.8 V_{RHE}, followed by Li-IrO_x, which shows a current density of ~55 mA cm^{-2} (see **Figure 4a**) at the same applied potential. In sharp contrast, r-IrO_2 shows the lowest activity amongst the electrocatalysts investigated, with a current density of 36 mA cm^{-2} at 1.8 V_{RHE}, consistent with previous findings.[19] The activities of the Na-IrO_x and K-IrO_x catalysts are intermediate, with the former showing a current density of 45 mA cm^{-2}, while the latter 35 mA cm^{-2} and therefore shows a similar performance to r-IrO_2. LSV curves also showed a first redox event occurs at ~0.8 V_{RHE} for $IrO_2 \cdot 2H_2O$ and ~0.9 V_{RHE} for Li-IrO_x and a second redox event at ~1.2 V_{RHE} for both samples, indicating low-energy Ir^{3+}/Ir^{4+} and Ir^{4+}/Ir^{5+} transitions occur at the surface, consistent with previous observations for amorphous iridium oxide and Li-IrO_x (see **Figure S3**).[19] Similar features are observed

for Na-IrO_x and K-IrO_x, albeit much less pronounced than the higher activity electrocatalysts suggesting lower activity surfaces. Finally, IrO_2 does not show any indication of such transitions occurring at potentials below ~1.45 V_{RHE} — *i.e.* the onset region for OER. This further indicates that r-IrO_2 exhibits a significantly lower redox activity, consistent with its poor activity towards OER, as discussed in previous reports.[19,34] To further assess the OER activity, the overpotentials at 10 mA cm^{-2} (η^{10}) have been determined. r-IrO_2, $IrO_2 \cdot 2H_2O$ and Li-IrO_x showed a η^{10} of 390 and 280 and 310 mV, respectively, whereas Na-IrO_x and K-IrO_x reached the benchmark current density at 350 and 360 mV, respectively. Iridium mass-normalised current densities confirm the same trends as the as-measured LSV curves (see **Figure 4b**).

OER activity was normalised against the roughness factor (R_f) obtained by electrochemically active surface area (ECSA) measurements (see **Figure S4**). ECSA values of 0.73, 0.16, 0.05, 0.15 and 0.41 cm^2 for r-IrO_2, $IrO_2 \cdot 2H_2O$, Li-IrO_x, Na-IrO_x and K-IrO_x, respectively, were determined through double layer capacitance methods. The R_f for each catalyst can be determined by dividing the ECSA by the electrode geometric area. The determined R_f values are 3.72, 0.83, 0.24, 0.77 and 2.08 for r-IrO_2, $IrO_2 \cdot 2H_2O$, Li-IrO_x, Na-IrO_x and K-IrO_x respectively. The activities normalised by R_f reveal that Li-IrO_x shows much higher normalised activity compared to the other electrocatalysts (see **Figure 4c**) showing a possible promotional effect of Li^+ in the OER catalysts compared to alkali metal-free systems. Tafel slopes were derived from semi-steady-state conditions obtained from linear sweep voltammetry (LSV) measurements performed at a scan rate of 0.5 mV s^{-1} (see **Figure 4d**). At low overpotentials, Tafel slopes were 38.8, 47.6, 54.7 and 59.2 mV dec^{-1} for $IrO_2 \cdot 2H_2O$, Li-IrO_x, Na-IrO_x and K-IrO_x respectively. These results are consistent with those observed from LSV curves, confirming the higher intrinsic activity of $IrO_2 \cdot 2H_2O$ and Li-IrO_x compared to the Na- and K-containing analogues.

In situ XAS during electrochemistry was conducted in 0.1M $HClO_4$ at a potential above and below the OER onset for each sample. As XAS is a bulk technique the formal oxidation state changes determined represent only the average oxidation states of the materials and changes are likely to only come from redox active sites at the surface or near-surface while the bulk remains largely unchanged. The Ir-L_3 edge of the catalyst series was measured after immobilisation onto carbon paper and immersion in the electrolyte. Compared to the as prepared samples the immersed catalysts showed lower white line positions as determined by the minimum in the second derivative. This suggests that when compared to the samples that have been dried before acquisition the amorphous and layered samples in electrolyte have a higher density of unoccupied states state due to hydration/protonation. An exception is r-IrO_2 which maintains a formal oxidation state close to Ir^{4+} consistent with its highly ordered structure which is less amenable to water penetration into the bulk or surface hydroxylation. Subsequently, the potential was increased to 1.4 $V_{Ag/AgCl}$ in 100 mV steps from 0.9 $V_{Ag/AgCl}$ to allow spectral acquisition at each potential. **Figure S5** shows the XANES spectra acquired in electrolyte with no applied potential and at 1.0 and 1.4 $V_{Ag/AgCl}$ to represent the state of the catalyst above and below the OER onset. On application

of potential the white line position of rutile IrO_2 remains unchanged indicating no significant observable change in bulk oxidation state above the OER onset. FT-EXAFS (see **Figure S5b**) shows no significant changes in the scattering intensity consistent with 1st shell Ir-O_6 or the 2nd coordination shell Ir-Ir. A summary of the fitting of the first shell, **Table 2,** is consistent with an Ir-O_x coordination of 5.6 ± 0.6 when under OER conditions with an Ir-O bond length of 1.98 Å (full fitting parameters are reported in **Table S2**). In contrast, on application of potential, commercial $IrO_2 \cdot 2H_2O$ demonstrates a shift in the white line position to higher energy indicating oxidation beyond r-IrO_2 and a corresponding change in Ir-O bond length from 2.02 to 1.96 Å consistent with a higher oxidation state Ir species and more facile redox processes observed in the LSV experiments. A reduction in Ir-O CN on polarisation suggests the formation of O-vacancies in the structure which have been reported to be both involved in the reaction mechanism and a trigger for dissolution and catalyst deactivation.[12] In contrast, the Li-IrO_x shows much less pronounced changes in polarisation, which could partly be ascribed to the lower ECSA compared to $IrO_2 \cdot 2H_2O$. On immersion in the electrolyte, only slight changes in CN and Ir-O bond length are observed despite the high activity of the sample, possibly suggesting that the activity in this sample is not strongly correlated to the formation of O-vacancy or that the structure has enhanced stability towards O-vacancy formation. The Na-IrO_x sample shows oxidation on the application of potential inferred from a shift in white line positions without significant changes in Ir-O CN or Ir-O bond length again suggesting OER activity without significant loss of Ir-O coordination.

The surface-sensitive spin-orbit split Ir 4f X-ray photoelectron spectra for the as-prepared samples in **Figure 5a** were fitted using the theory-based model developed by Pfeifer *et al*. and summarised in **Table S3**.[35,36] A peak with a maximum at 61.7 eV and Doniach-Ŝunjić (DS) lineshape together with the associated shake-up satellites ~1.0 eV higher in binding energy (BE) is consistent with the $Ir4f_{5/2}$ component of Ir^{IV} in rutile IrO_2. An additional DS component at 62.4 eV BE (~7 eV upshifted from Ir^{IV} in rutile IrO_2) was also observed and an associated satellite peak which cannot be unequivocally assigned based on existing literature. A peak at 5 eV higher BE than Ir^{IV} was earlier associated with bulk Ir^{III}.[37] However, recently, Ir surface species with a formal oxidation state > 5 bound to μ_1-O on (110) terraces or μ_1-OH on (111) terraces of IrO_2 surfaces were suggested to contribute to this feature.[38] Consistently with L_3-edge XANES and XRD analysis, Ir 4f XPS shows that Li-IrO_x is the sample that least resembles the electronic surface structure of rutile-type IrO_2. In analogy to previous computed XPS using the surface model fit, one could postulate that differences are related to a higher abundance of protonated oxygen-bearing Ir-octahedra species. The O1s XPS spectra of the as-prepared samples are depicted in **Figure 5b**. The fitting includes 6 components as summarised in **Supporting Table 3**, between 529.1 -533.6 eV. In terms of assignments, M-O species with O in a formal oxidation state -2 contribute to the spectra below 531 eV, whereas above this BE, hydroxylated and carbonated species are found.[39] Thus, it can be concluded that the Li-IrO_x surface is dominated by surface hydroxylated species, whereas both Na- and K-containing samples present a majority of M-O species consistent with

the larger crystallites found for these samples. The additional peak at 529.5 eV in Na- and Li- compared to K- indicates a coexistence of different metal-O bonds beside the rutile-type Ir-O_6 bonds. According to literature this component is inconsistent with any of the possible Li-O(H), Na-O(H) and K-O(H) bonds and therefore likely related to an Ir-O bond in a different environment than rutile-type Ir-O_6 bonds. The O K-edge NEXAFS is highly diagnostic to differentiate O species and identify features related to high OER activity.[40,41] The O K-edge for the samples, **Figure S6,** shows the 528-534 eV region which represents the 1s $\rightarrow$ O2p hybridized with 5d metal states which have t_{2g}-e_g symmetry. Both Auger electron yield (AEY) and total electron yield (TEY) spectra show that the pre-edge peaks differ significantly in relative intensity among the samples. Commercial rutile-type IrO_2 (r-IrO_2) is characterized by resonances at ~529 eV and ~530 eV , associated with bulk μ_2-O and μ_3-O, respectively. While the latter is typical in rutile IrO_2, the former is not typically found in highly crystalline rutile IrO_2. A μ_2-O ~529 eV is associated to Ir^{III} in the bulk and is shifted to higher energy when protonated. Consistent with earlier work, this resonance is predominant in the pre-edge region of the O K-edge of Li-IrO_x, and is convoluted with the μ_3-O resonance, which presents lower intensity compared to r-IrO_2. Na-IrO_x presents mainly the μ_2-O resonance, indicating that this is the predominant species in the layered oxide structures. A correlation can be drawn between the population of O species and the energy of the Ir L_3-edge (inset Figure 3a) as well as the Ir-O distance. For the commercial r-IrO_2 the white line shifts to higher energy compared to the other materials studied, consistent with a shorter Ir-O bond and a μ_3-O resonance in the O K-edge spectrum. K-IrO_x is characterized by two well resolved pre-edge peaks, with a resonance consistent with μ_3-O species, whereas a lower energy resonance is shifted to higher energy than μ_2-O, possibly due to protonantion (μ_2-OH). The pre-edge is almost absent in $IrO_2 \cdot 2H_2O$ in AEY, while in TEY presents resonances at energies similar to K-IrO_x, although, the relative intensity of the two resonance is the opposite. A decrease of the intensity is in general observed when the bond covalency is low (O2p-t_{2g} hybridisation) and the ionic character is high. The broad resonance above 537 eV reflects the Ir-O bond distance distribution. Peak maxima at lower energy for Li-IrO_x and $IrO_2 \cdot 2H_2O$ and to a lesser extent for Na-IrO_x and K-IrO_x indicate longer Ir-O bonds than r-IrO_2, consistent with the L_3-edge EXAFS data (Figure S3). It is possible to postulate that the intercalation of Li^+ , Na^+ and K^+ between the IrO_6-layers is reflected in the elongation of Ir-O bonds pointing towards the interlayer space as well as an increase of the ionic character of this bond.

The stability of the electrocatalysts was assessed *via* chronopotentiometry at a benchmark current density of 10 mA cm^{-2}. All the *M*-IrO_x samples (*M* = Li^+, Na^+ and K^+) showed good stability over 2 h with no evidence of degradation, while the commercially available amorphous $IrO_2 \cdot 2H_2O$ showed deactivation within the first ~30 minutes of operation, with the results for $IrO_2 \cdot 2H_2O$ and Li-IrO_x consistent with previous findings,[19] and showing that the layered catalysts indeed offer potentially more durable alternatives to amorphous iridium oxide (see **Figure 6**). Longer tests at the benchmark current, *i.e.* 10 mA cm^{-2}, have revealed that the *M*-IrO_x electrocatalysts can sustain longer periods of operation

and suggest that Li-, Na- and K-IrO_x can operate for up to ~22, ~15 and ~8 h , respectively, outperforming commercial r-IrO_2 and $IrO_2 \cdot 2H_2O$ inks prepared in the same way (see **Figure 7**).

Conclusions

It was previously shown that residual Li^+ suppresses the formation of crystalline rutile IrO_2 during mild heat treatment (~500 °C) of amorphous iridium oxyhydroxides, leading to a nanocrystalline lithium iridate which is more active compared to rutile IrO_2 synthesied in the absence of Li^+ at similar temperatures. Such an iridate has shown comparable activity to amorphous iridium oxyhydroxides and improved durability. We focused on synthesising sodium and potassium-containing analogues, namely Na-IrO_x and K-IrO_x, using a similar mild heat treatment method. We demonstrate that incorporating interlayer alkali metal cations into layered iridium oxides provides a route to obtain materials with enhanced activity compared to rutile IrO_2 with higher stability. In particular, Li-IrO_x, Na-IrO_x and K-IrO_x outperform r-IrO_2 albeit the measured activity decreases with larger cations, *i.e.* $Li^+ > Na^+ > K^+$. Despite this, they have been shown to withstand electrocatalytic conditions in acidic media for more than 15 h compared to commercial r-IrO_2 and $IrO_2 \cdot 2H_2O$ which are stable for <1 h under the same experimental conditions. These results have further confirmed that layered structures could allow for orthogonality between activity and stability, with stability being the most significant limitation for the fabrication of industrial PEM electrocatalysts.

Acknowledgemnts

We are grateful for support from the UK Catalysis Hub funded by EPSRC grant reference EP/R026645/1. We are grateful to Diamond Light Source for providing instrument time and support for the B07 (SI35991) and B18 beamlines (SP33143-1). We want to thank Dr D. Morgan (Cardiff University, UK) for carrying out XPS work through the support of the EPSRC National Facility for X-ray photoelectron spectroscopy ('HarwellXPS', EP/Y023587/1, EP/Y023609/1, EP/Y023536/1, EP/Y023552/1 and EP/Y023544/1). We are grateful to Dr J. Yang (College of International Education, ECUST, Shanghai, China) for providing us with the crystallographic model for $K_{0.3}IrO_2 \cdot 0.6H_2O$. We would also like to thank Johnson Matthey for providing us with precursors for our synthesis and for conducting ICP measurements on our samples. We thank Dr M. E. Schuster (Johnson Matthey) for carrying out the HR-TEM measurements. Part of the illustrations in scheme 1 were created using Chemix.

10.1002/cctc.202401326

Figure 1 - Powder X-ray diffraction patterns and corresponding Le Bail refinement of layered IrO_x structures (a-b) Li-IrO_x (c-d) Na-IrO_x (e-f) K-IrO_x. The black crosses, red and green lines in the refinements are experimental, calculated intensities and difference curve, respectively. Vertical markers indicate the position of the expected Bragg reflections.

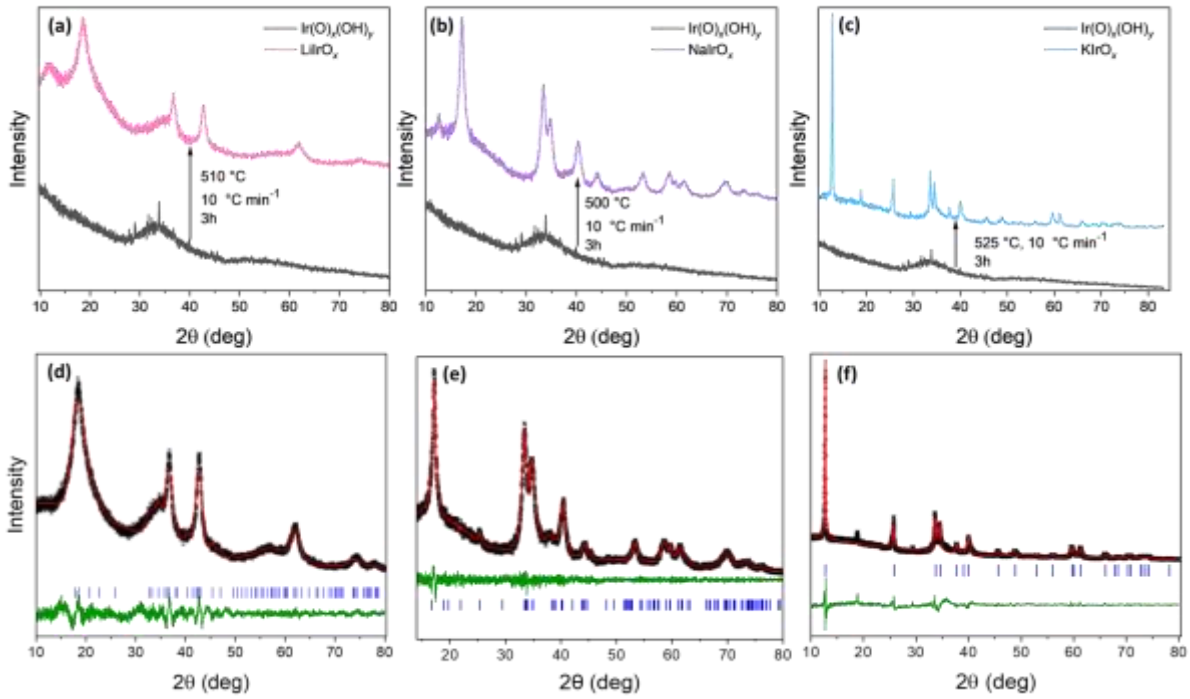

10.1002/cctc.202401326

Figure 2 - SEM and HR-TEM images, showing nanocrystalline domains, for (a,d) Li-IrO_x, (b,e) Na-IrO_x, in (c,f) K-IrO_x, suggesting higher crystallinity for the latter compound.

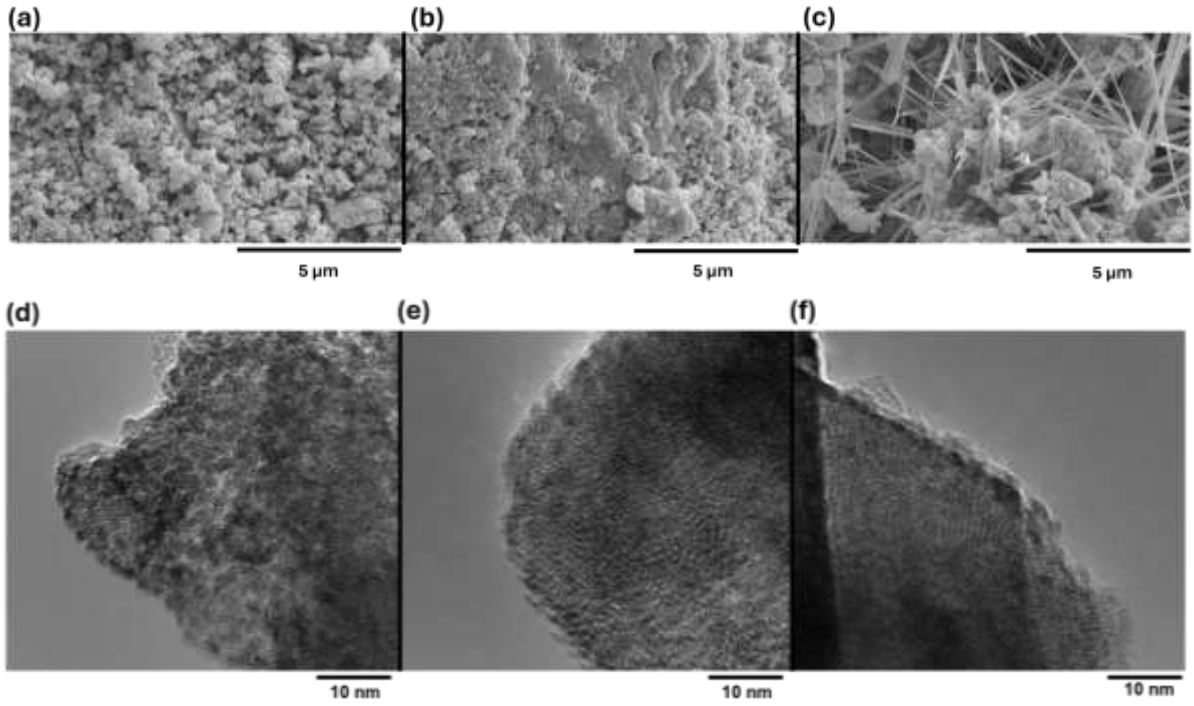

10.1002/cctc.202401326

Figure 3 – a) Transmission Ir-L_3-edge XANES and b) Fourier transformed EXAFS of commercial rutile IrO_2 and amorphous $IrO_2 \cdot 2H_2O$ and synthesised Li^+, Na^+ and K^+ iridates.

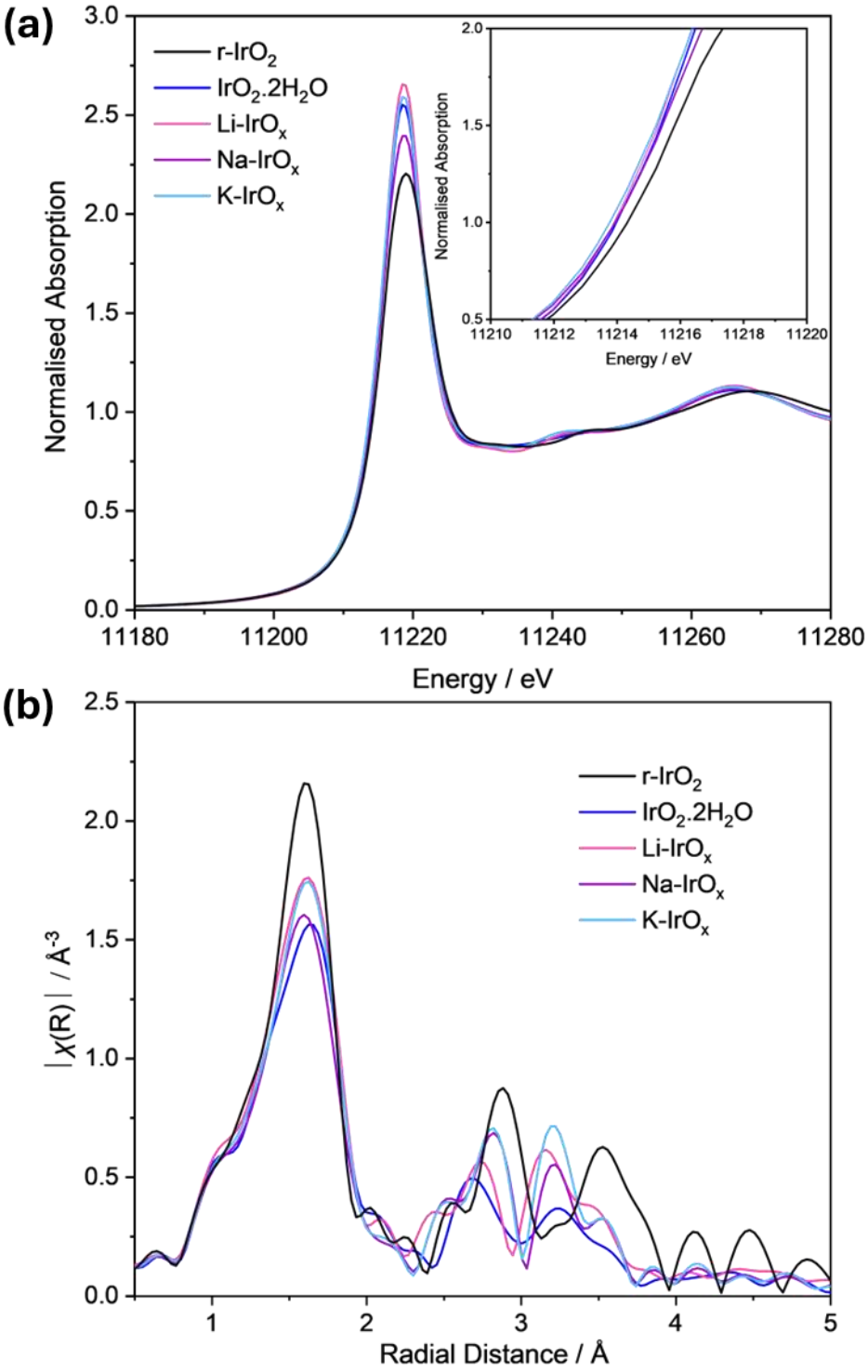

10.1002/cctc.202401326

Table 1 – EXAFS model fitting parameters for first shell Ir-O of catalysts measured at the Ir-L_3based on IrO_2 [ICSD 56009] and with floated CN and R. Fitted data range k 3-12 and R 1.5 – 2.5 Å.

sample	scattering path	CN	R (Å)	$2\sigma^2$ (Å^2)	S^2	E_f (eV)	R_{factor} + reduced-χ^2
r-IrO_2	Ir−O	5.8 ± 0.3	1.97 ± 0.01	0.002(4)	0.79*	10.3 ± 0.6	0.030 (734)
$IrO_2 \cdot 2H_2O$	Ir−O	6.0 ± 0.6	2.00 ± 0.01	0.005(1)	0.79*	10.0 ±1.2	0.008 (6122)
Li-IrO_x	Ir−O	6.2 ± 0.6	1.99 ± 0.02	0.005(1)	0.79*	9.9 ± 1.3	0.004 (8937)
Na-IrO_x	Ir−O	5.9 ± 0.3	1.99 ± 0.01	0.004(5)	0.79*	9.7 ± 0.6	0.012(4204)
K-IrO_x	Ir−O	6.0 ± 0.4	1.99 ± 0.02	0.004(3)	0.79*	9.8 ± 0.8	0.012 (5676)

* S_o^2 fixed at a value of 0.79 determined by fitting Iridium chloride as a standard with a fixed CN = 6.

10.1002/cctc.202401326

Figure 4 - (a) As-measured, (b) mass-normalised and (c) roughness factor-normalised current densities of commercial IrO_2 standards and synthesised *M*-IrO_x catalysts (*M* = Li^+, Na^+, K^+) measured by LSV (0.2 – 1.8 V_{RHE} at 5 mV s^{-1}, RDE at 2500 rpm). Shadowed areas in Figure A represent standard deviations over multiple LSV measurements. (d) Tafel plots at low overpotential obtained from the linear region of LSV polarization curves at 0.5 mV·s^{-1}

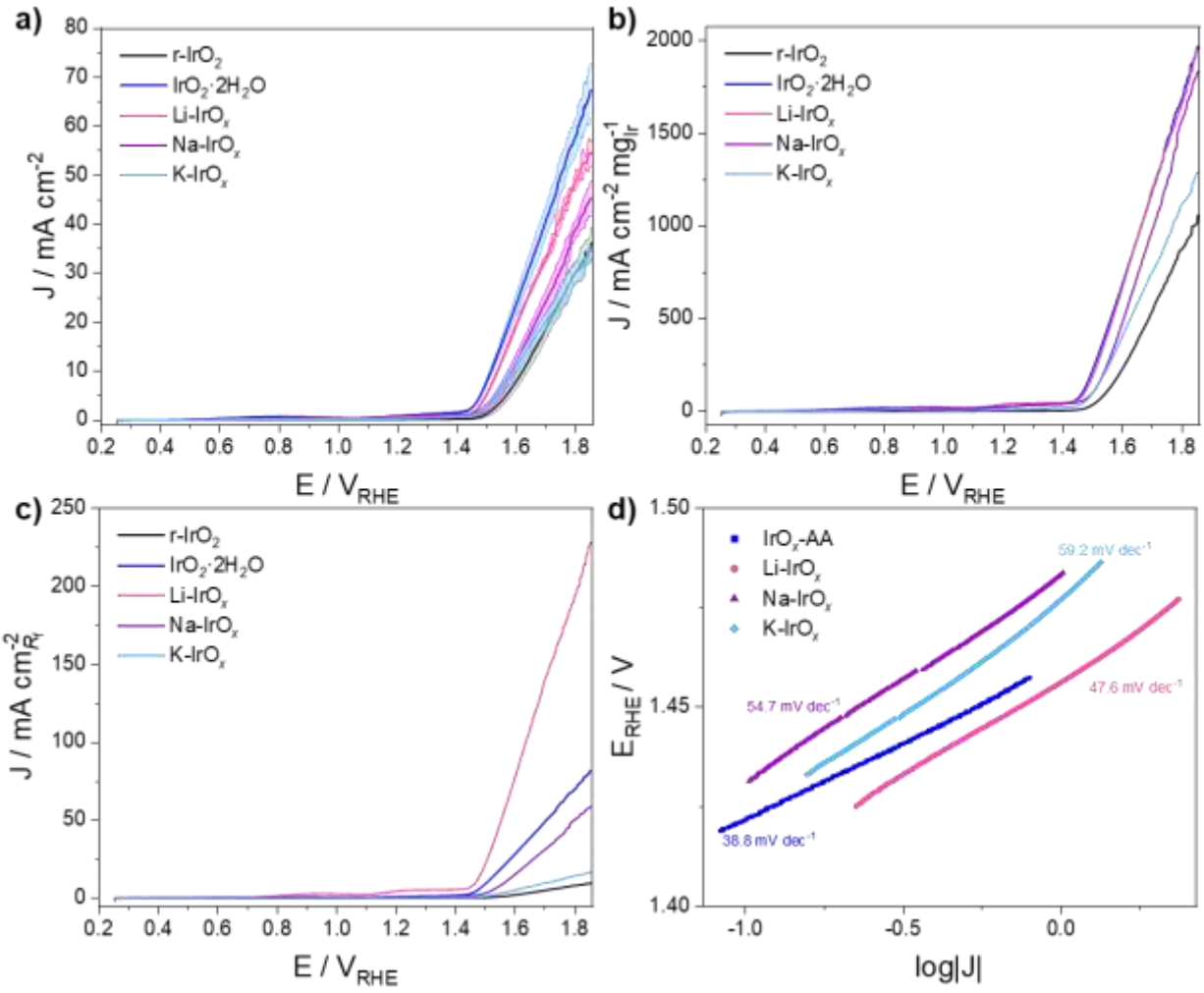

10.1002/cctc.202401326

Table 2 – Summary of EXAFS fitting for *in situ* experiment

sample	Conditions	Ir-O_x CN	R (Å)	White Line Position / eV	Average Oxidation State
r-IrO_2	In electrolyte	5.8 ± 0.8	1.98 ± 0.01	11218.3	3.8
	1.4$V_{Ag/AgCl}$	5.6 ± 0.6	1.98 ± 0.01	11218.3	3.8
$IrO_2 \cdot 2H_2O$	In electrolyte	5.4 ± 0.5	2.02 ± 0.01	11217.9	3.5
	1.4$V_{Ag/AgCl}$	5.1 ± 0.5	1.96 ± 0.01	11219.0	4.5
Li-IrO_x	In electrolyte	6.1 ± 0.6	2.02 ± 0.01	11217.6	3.2
	1.4$V_{Ag/AgCl}$	5.8 ± 0.7	2.01 ± 0.01	11217.8	3.4
Na-IrO_x	In electrolyte	5.7 ± 1.2	2.03 ± 0.02	11217.4	3.0
	1.4$V_{Ag/AgCl}$	5.5 ± 0.4	2.02 ± 0.01	11218.4	3.9
K-IrO_x	In electrolyte	5.4 ± 1.4	2.01 ± 0.02	11217.8	3.4
	1.4$V_{Ag/AgCl}$	5.8 ± 0.6	1.97 ± 0.01	11218.5	4.0

* S_o^2 fixed at a value of 0.79 determined by fitting Iridium chloride as a standard with a fixed CN = 6.

10.1002/cctc.202401326

Figure 5 – Fitted Ir 4f (left) and O1s (right) XPS spectra for Li-IrO_x, Na-IrO_x and K-IrO_x obtained in UHV.

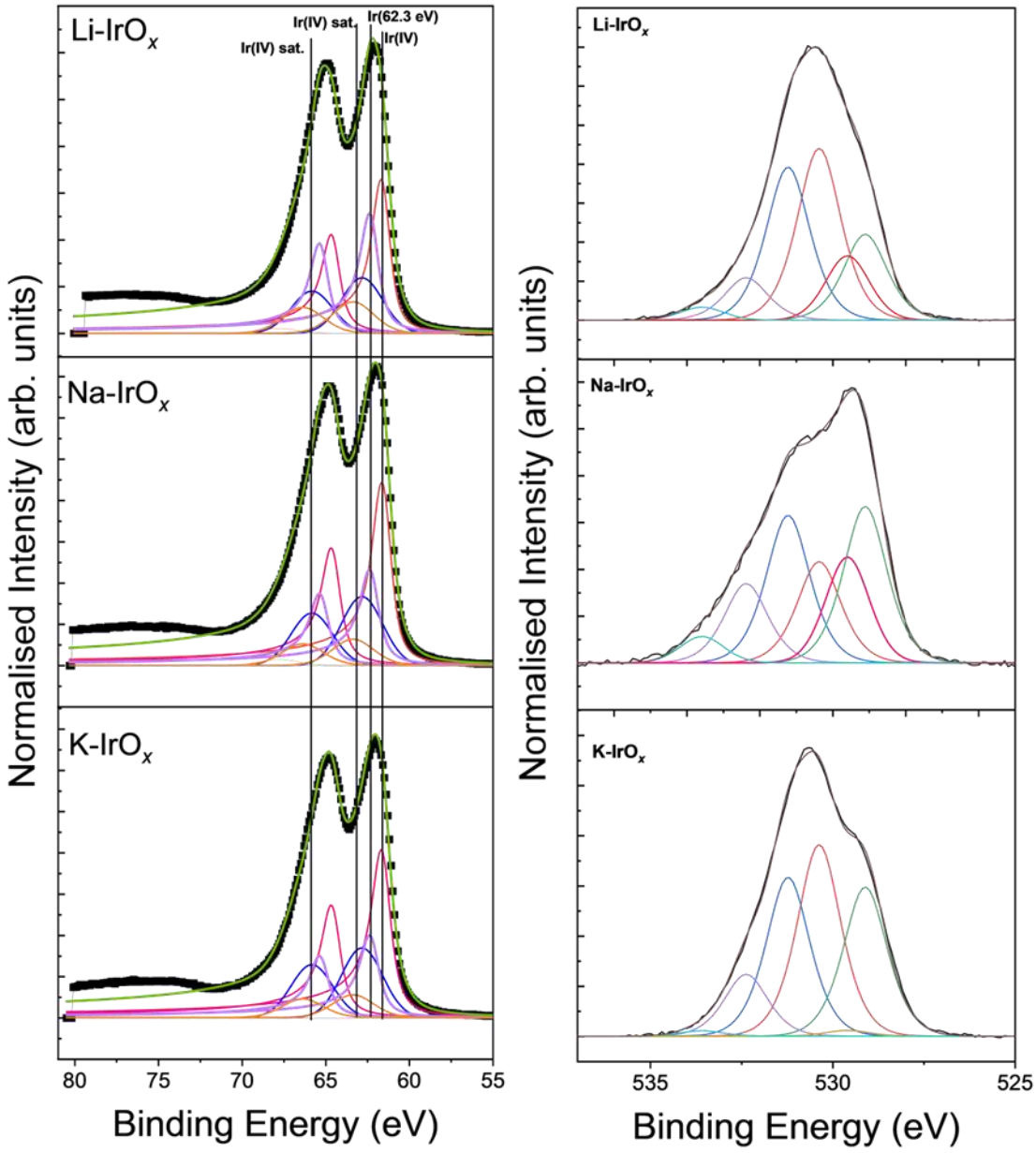

10.1002/cctc.202401326

Figure 6 - Stability of electrocatalysts assessed *via* chronopotentiometry (2 h at 10 mA cm^{-2}).

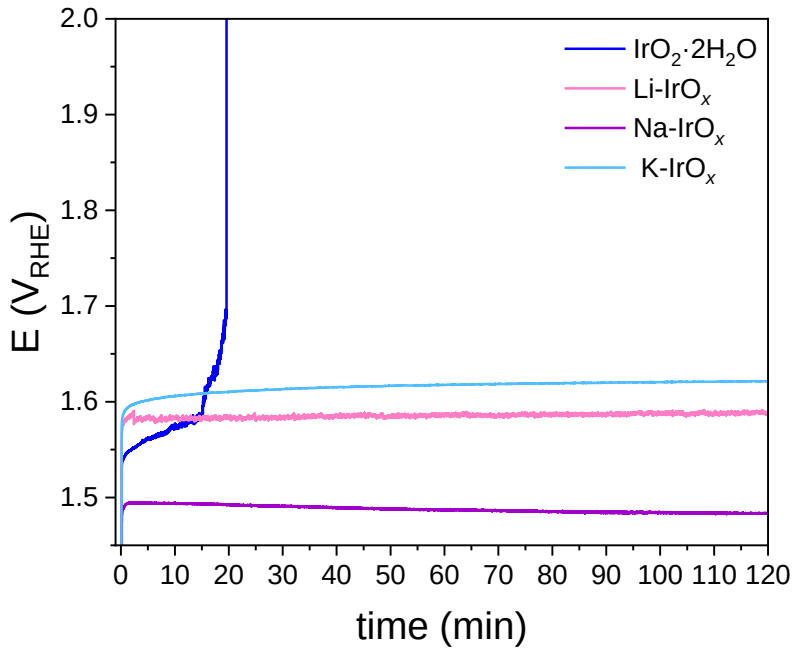

Figure 7: Stability of electrocatalysts assessed *via* chronopotentiometry for longer acquisition times (25 h at 10 mA cm^{-2}).

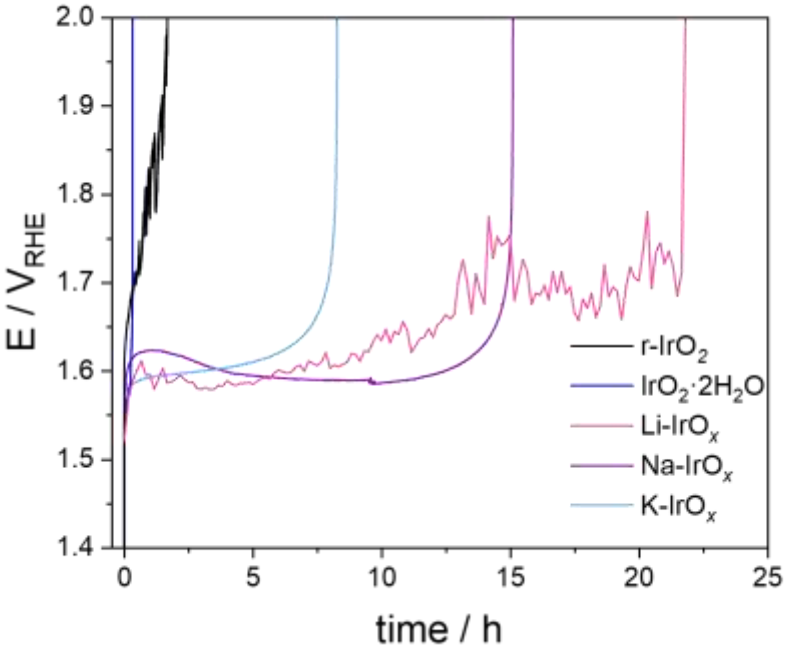

References

1 O. Schmidt, A. Gambhir, I. Staffell, A. Hawkes, J. Nelson and S. Few, *Int. J. Hydrog. Energy*, 2017, **42**, 30470–30492.
2 S. Shiva Kumar and V. Himabindu, *Mater. Sci. Energy Technol.*, 2019, **2**, 442–454.
3 D. Hochfilzer, I. Chorkendorff and J. Kibsgaard, *ACS Energy Lett.*, 2023, **8**, 1607–1612.
4 T. Naito, T. Shinagawa, T. Nishimoto and K. Takanabe, *Inorg. Chem. Front.*, 2021, **8**, 2900–2917.
5 H. Jang and J. Lee, *J. Energy Chem.*, 2020, **46**, 152–172.
6 C. Wang, F. Lan, Z. He, X. Xie, Y. Zhao, H. Hou, L. Guo, V. Murugadoss, H. Liu, Q. Shao, Q. Gao, T. Ding, R. Wei and Z. Guo, *ChemSusChem*, 2019, **12**, 1576–1590.
7 Y. Zhang, X. Zhu, G. Zhang, P. Shi and A.-L. Wang, *J. Mater. Chem. A*, 2021, **9**, 5890–5914.
8 F. Bizzotto, M. Arenz and J. Quinson, *Mater. Lett.*, 2022, **308**, 131209.
9 S. Cherevko, S. Geiger, O. Kasian, A. Mingers and K. J. J. Mayrhofer, *J. Electroanal. Chem.*, 2016, **774**, 102–110.
10 S. Geiger, O. Kasian, B. R. Shrestha, A. M. Mingers, K. J. J. Mayrhofer and S. Cherevko, *J. Electrochem. Soc.*, 2016, **163**, F3132–F3138.
11 K. Schweinar, B. Gault, I. Mouton and O. Kasian, *J. Phys. Chem. Lett.*, 2020, **11**, 5008–5014.
12 O. Kasian, J. Grote, S. Geiger, S. Cherevko and K. J. J. Mayrhofer, *Angew. Chem. Int. Ed.*, 2018, **57**, 2488–2491.
13 S. Cherevko, S. Geiger, O. Kasian, N. Kulyk, J.-P. Grote, A. Savan, B. R. Shrestha, S. Merzlikin, B. Breitbach, A. Ludwig and K. J. J. Mayrhofer, *Catal. Today*, 2016, **262**, 170–180.
14 M. Falsaperna, R. Arrigo, F. Marken and S. J. Freakley, *ChemElectroChem*, 2024, e202300761.
15 O. van der Heijden, J. J. J. Eggebeen, H. Trzesniowski, N. Deka, R. Golnak, J. Xiao, M. van Rijn, R. V. Mom and M. T. M. Koper, *Angew. Chem. Int. Ed.*, 2024. **63**, e202318692.
16 J. R. Esquius, D. J. Morgan, I. Spanos, D. G. Hewes, S. J. Freakley and G. J. Hutchings, *ACS Appl. Energy Mater.*, 2020, **3**, 800–809.
17 J. Gao, C. Q. Xu, S. F. Hung, W. Liu, W. Cai, Z. Zeng, C. Jia, H. M. Chen, H. Xiao, J. Li, Y. Huang and B. Liu, *J. Am. Chem. Soc.*, 2019, **141**, 3014–3023.
18 W. Sun, Y. Song, X.-Q. Gong, L. Cao and J. Yang, *ACS Appl. Mater. Interfaces*, 2016, **8**, 820–826.
19 J. Ruiz Esquius, D. J. Morgan, G. Algara Siller, D. Gianolio, M. Aramini, L. Lahn, O. Kasian, S. A. Kondrat, R. Schlögl, G. J. Hutchings, R. Arrigo and S. J. Freakley, *J. Am. Chem. Soc.*, 2023, **145**, 6398–6409.
20 D. C. Grinter, F. Venturini, P. Ferrer, M. A. Van Spronsen, R. Arrigo, W. Quevedo Garzon, K. Roy, A. I. Large, S. Kumar and G. Held, *Synchrotron Radiat. News*, 2022, **35**, 39–47.
21 B. Ravel and M. Newville, *J. Synchrotron Radiat.*, 2005, **12**, 537–541.
22 P. E. Pearce, C. Yang, A. Iadecola, J. Rodriguez-Carvajal, G. Rousse, R. Dedryvère, A. M. Abakumov, D. Giaume, M. Deschamps, J. M. Tarascon and A. Grimaud, *Chem. Mater.*, 2019, **31**, 5845–5855.
23 F. Freund, S. C. Williams, R. D. Johnson, R. Coldea, P. Gegenwart and A. Jesche, *Sci. Rep.*, 2016, **6**, 35362.
24 C. Yang, G. Rousse, K. Louise Svane, P. E. Pearce, A. M. Abakumov, M. Deschamps, G. Cibin, A. V. Chadwick, D. A. Dalla Corte, H. Anton Hansen, T. Vegge, J.-M. Tarascon and A. Grimaud, *Nat. Commun.*, 2020, **11**, 1378–1378.
25 F. Gonell, G. Rousse, M. Odziomek, W. Baaziz, O. Ersen, A. Grimaud and C. Sanchez, *ACS Appl. Nano Mater.*, 2023, **6**, 2577–2584.
26 M. J. O'Malley, H. Verweij and P. M. Woodward, *J. Solid State Chem.*, 2008, **181**, 1803–1809.
27 A. L. Bail, H. Duroy and J. L. Fourquet, *Mater. Res. Bull.*, 1988, **23**, 447–452.
28 S. K. Choi, R. Coldea, A. N. Kolmogorov, T. Lancaster, I. I. Mazin, S. J. Blundell, P. G. Radaelli, Y. Singh, P. Gegenwart, K. R. Choi, S.-W. Cheong, P. J. Baker, C. Stock and J. Taylor, *Phys. Rev. Lett.*, 2012, **108**, 127204–127204.
29 L. Zhu, C. Ma, L. Cao and J. Yang, *ACS Appl. Energy Mater.*, 2023, **6**, 4757–4765.
30 F. T. L. Muniz, M. A. R. Miranda, C. Morilla Dos Santos and J. M. Sasaki, *Acta Crystallogr. Sect. Found. Adv.*, 2016, **72**, 385–390.

31 A. H. Reksten, A. E. Russell, P. W. Richardson, S. J. Thompson, K. Mathisen, F. Seland and S. Sunde, *Phys. Chem. Chem. Phys.*, 2020, **22**, 18868–18881.
32 A. M. Cruz, Ll. Abad, N. M. Carretero, J. Moral-Vico, J. Fraxedas, P. Lozano, G. Subías, V. Padial, M. Carballo, J. E. Collazos-Castro and N. Casañ-Pastor, *J. Phys. Chem. C*, 2012, **116**, 5155–5168.
33 E. Oakton, D. Lebedev, M. Povia, D. F. Abbott, E. Fabbri, A. Fedorov, M. Nachtegaal, C. Copéret and T. J. Schmidt, *ACS Catal.*, 2017, **7**, 2346–2352.
34 Y. Lee, J. Suntivich, K. J. May, E. E. Perry and Y. Shao-Horn, *J. Phys. Chem. Lett.*, 2012, **3**, 399–404.
35 J. J. Velasco-Vélez, T. E. Jones, V. Streibel, M. Hävecker, C.-H. Chuang, L. Frevel, M. Plodinec, A. Centeno, A. Zurutuza, R. Wang, R. Arrigo, R. Mom, S. Hofmann, R. Schlögl and A. Knop-Gericke, *Surf. Sci.*, 2019, **681**, 1–8.
36 V. Pfeifer, T. E. Jones, J. J. Velasco Vélez, C. Massué, M. T. Greiner, R. Arrigo, D. Teschner, F. Girgsdies, M. Scherzer, J. Allan, M. Hashagen, G. Weinberg, S. Piccinin, M. Hävecker, A. Knop-Gericke and R. Schlögl, *Phys. Chem. Chem. Phys.*, 2016, **18**, 2292–2296.
37 V. Pfeifer, T. E. Jones, J. J. Velasco Vélez, R. Arrigo, S. Piccinin, M. Hävecker, A. Knop-Gericke and R. Schlögl, *Chem. Sci.*, 2017, **8**, 2143–2149.
38 J.-J. Velasco-Vélez, E. A. Carbonio, C.-H. Chuang, C.-J. Hsu, J.-F. Lee, R. Arrigo, M. Hävecker, R. Wang, M. Plodinec, F. R. Wang, A. Centeno, A. Zurutuza, L. J. Falling, R. V. Mom, S. Hofmann, R. Schlögl, A. Knop-Gericke and T. E. Jones, *J. Am. Chem. Soc.*, 2021, **143**, 12524–12534.
39 R. Arrigo, R. Blume, V. Streibel, C. Genovese, A. Roldan, M. E. Schuster, C. Ampelli, S. Perathoner, J. J. Velasco Vélez, M. Hävecker, A. Knop-Gericke, R. Schlögl and G. Centi, *ACS Catal.*, 2022, **12**, 411–430.
40 N. Diklić, A. H. Clark, J. Herranz, D. Aegerter, J. S. Diercks, A. Beard, V. A. Saveleva, P. Chauhan, M. Nachtegaal, T. Huthwelker, D. Lebedev, P. Kayser, J. A. Alonso, C. Copéret and T. J. Schmidt, *ACS Catal.*, 2023, **13**, 11069–11079.
41 J. Marniemi and M. G. Parkki, *Biochem. Pharmacol.*, 1975, **24**, 1569–1572.